ACS APPLIED MATERIALS & INTERFACES

www.acsami.org

Research Article

Strategy of Voltage Match on the Maximum Power Point for a High-Efficiency Photorechargeable Device

Binglin Guo, Yongyue Li, Yihao Gao, Shengnan Zhao, Yingfeng Li, Xiaojun Lv, Changhua Mi, and Meicheng Li*

Cite This: *ACS Appl. Mater. Interfaces* 2023, 15, 11875−11884

Read Online

ACCESS | Metrics & More | Article Recommendations | Supporting Information

ABSTRACT: A photorechargeable device can generate power from sunlight and store it in one device, which has a broad application prospect in the future. However, if the working state of the photovoltaic part in the photorechargeable device deviates from the maximum power point, its actual power conversion efficiency will reduce. The strategy of voltage match on the maximum power point is reported to achieve a high overall efficiency (η_{oa}) of the photorechargeable device assembled by a passivated emitter and rear cell (PERC) solar cell and Ni-based asymmetric capacitors. According to matching the voltage of the maximum power point of the photovoltaic part, the charging characteristics of the energy storage part are adjusted to realize a high actual power conversion efficiency of the photovoltaic part (η_{pv}). The η_{pv} of a $Ni(OH)_2$-rGO-based photorechargeable device is 21.53%, and the η_{oa} is up to 14.55%. This strategy can promote further practical application for the development of photorechargeable devices.

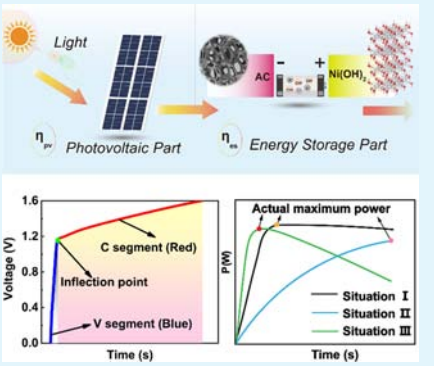

KEYWORDS: *photorechargeable device, strategy of voltage match, high overall efficiency, Ni-based asymmetric capacitors, PERC solar cell*

Downloaded via NORTH CHINA ELECTRIC POWER UNIV on March 9, 2023 at 01:19:27 (UTC).
See https://pubs.acs.org/sharingguidelines for options on how to legitimately share published articles.

1. INTRODUCTION

The energy crisis will be one of the greatest challenges in the next 50 years.[1] With the growing demand for energy in the industrial system, fossil fuels, as the main source of energy, have been increasingly depleted, which requests the vigorous development of renewable energy. At the same time, the environmental pollution and greenhouse effect caused by the consumption of fossil fuels are the main concerns of environmental protection policies.[2] As a kind of renewable energy, solar energy is clean and pollution-free, which is an effective means to solve the energy crisis. There is as much as 1×10^5 TW·h^{-1} of solar energy received on the surface of the earth, which can fully meet the global annual energy consumption demand of 16 TW.[3] However, solar energy varies in different regions at different times.[2,4] Meanwhile, the energy fluctuation converted from solar energy leads to the contradiction between energy supply and demand.[5] To balance the contradiction, the converted solar energy needs to be stored in other energy storage equipment.[6,7] Therefore, it is necessary to develop an integrated device to collect and store solar energy. A photorechargeable device (PRD) is a kind of equipment that realizes photovoltaic and energy storage functions in one device through structural simplification or structural design. A considerable number of research studies have been reported on PRDs, which can be mainly divided into simplified devices (SDs) and complete devices (CDs). An SD has an electrode shared with functions of light to electric conversion and energy storage. Such devices usually contain only two working electrodes, and some photoelectrochemical devices can also be classified into this category. The research on SDs has made great contributions to structural innovation and mechanism exploration for the development of the PRD.[8−13] But limited by low efficiency and stability, the practicability of SDs has a lot of room for improvement.[6,14] A CD refers to a device with one working electrode at least for energy storage or light to electric conversion only, which usually includes three or four electrodes.[15]

The device with a complete photovoltaic and energy storage structure is easier to obtain high efficiency while maintaining good stability compared to the SD. However, the mismatch between photovoltaic (PV) and energy storage (ES) parts leads to the degradation of device performance.[16,17] The overall efficiency (η_{oa}) of the CD is mainly limited by three aspects: voltage matching, current matching (rate capability matching), and maximum power point matching (efficiency matching). Compared with the fully charged voltage of ES devices such as supercapacitors and lithium-ion batteries, a single PV device usually has a low output voltage. ES devices need to be charged at low current to obtain higher energy efficiency. Therefore, ES devices require charging with high

Received: December 24, 2022
Accepted: February 9, 2023
Published: February 21, 2023

ACS Publications

© 2023 American Chemical Society

voltage and low current, while the PV device supply a power with low voltage and high current. The direct connection of the PV and ES devices leads to a series of problems, for example, the ES devices cannot be fully charged,[18] and the low η_{oa} of the PRD is caused by an excessive charge rate.[19] It is worth noting that adding a converter can solve the mismatch between the PV device and ES device of current and voltage.[20,21] However, it will lead to the enlargement of the device volume and the increasing of power dissipation. Additionally, there are many inconveniences, such as the difficulty of manufacturing flexible devices and the need of independent power supply for the converter. Especially for ultrasmall or ultralow power devices, the use of converters greatly limits the structural design and the η_{oa}.

The PRD does not work stably at the maximum power point during the photocharging process, resulting in a low η_{oa}, which has been pointed out in some research studies. Jin et al.[22] contributed an integrated flow battery combining a photoelectrode and redox flow battery. They proposed that controlling the formal cell potential of a redox flow battery and the $J-V$ characteristic of a solar cell can achieve voltage match. Wang et al.[23] integrated a perovskite solar module (PSM) and an aluminum-ion battery (AIB) on a dual-function aluminum electrode to prepare a solar rechargeable system. By rationally matching the maximum power point voltage of PSM with the AIB charging voltage, the solar-charging efficiency is 15.2% and the overall photoelectric conversion and storage efficiency is 12.04%. It made a significant contribution to the high η_{oa} by adjusting the ratio of the PV device maximum power point voltage to the maximum voltage of the ES device close to 1.[24] Huang et al.[25] employed a silicon solar cell as the PV unit for charging a $Ni(HCO_3)_2$-based hybrid supercapacitor, which is voltage adjustable. By changing the mass of the cathode, the fully charged voltage can be controlled. So that the maximum power point voltage of the PV device matches the fully charged voltage of the ES device. Agbo et al.[26] used a thin-film silicon solar cell and lithium-ion cell combined for portable electronic devices. The as-prepared device reported a solar energy-to-battery charging efficiency of 8.5% at the maximum power point. The above works have proposed that the matching of the maximum power point voltage and fully charged voltage of the ES part can improve the η_{oa} of the PRD. According to the working properties of PV and ES parts, it will be of a great guiding value for the selection and construction of the PRD if the specific voltage relationship is offered to realize the PRD working near the maximum power point during photocharging.

In this work, a passivated emitter and rear cell (PERC) solar cell was used as the PV part, and Ni-based asymmetric capacitors were used as the ES part to prepare the PRD. By adjusting the charging characteristics of the ES part to control the working state of the PV part, the usage of the strategy of voltage match on the maximum power point (SVM) can efficiently improve the power conversion efficiency. As a result, the highest η_{oa} of 14.55% is obtained. The PRD reached a near-maximum power state in only 0.4 s, and the η_{pv} takes 87.27% of the maximum power conversion efficiency (MPCE). The research shows that SVM can significantly improve the η_{oa}, which promotes the development and practical application of the PRD.

2. EXPERIMENTAL SECTION

2.1. Synthesis of $Ni(OH)_2$-rGO Composites. $Ni(OH)_2$-rGO composites were synthesized by a hydrothermal method using $NiSO_4 \cdot 6H_2O$, NaOH, and GO. Briefly, the weighed GO was ultrasonically dispersed in 100 mL of deionized water. The weighed $NiSO_4 \cdot 6H_2O$ and 20 mL of NaOH solution were added, fully stirred, and then transferred into a stainless steel autoclave lined with polytetrafluoroethylene. The mixture was heated to 180 °C to react for 7 h and cooled naturally. Finally, the product was filtered and freeze-dried to obtain $Ni(OH)_2$-rGO composites. By adjusting the ratio of raw materials, the mass ratio of GO to $Ni(OH)_2$ was 1:1, 1:2, and 1:5, and the products were, respectively, named GN1, GN2, and GN3. Pure $Ni(OH)_2$ powder without GO was prepared by the same method as the controls and named NH.

2.2. Characterization Methods. A scanning electron microscope (SEM, SU8100, HITACHI) was used to characterize the morphology of the prepared materials. X-ray diffraction (XRD, D8 Focus, Bruker) was used to analyze their phase and crystal structures.

2.3. Electrode Fabrication and Electrochemical Measurements. The active material, acetylene black, and PTFE were mixed into a slurry according to the ratio of 8:1:1 and coated on a nickel foam collector to prepare the working electrode. The electrochemical tests were conducted in a three-electrode system with Hg/HgO as the reference electrode and Pt as the counter electrode. Cyclic voltammetry (CV) tests were carried out in the potential range of 0−0.55 V at different scan rates. Galvanostatic discharge (GD) tests were completed at different current densities. The electrochemical impedance spectroscopy (EIS) curves were obtained at an open-circuit potential (OCP) with a frequency range of 100 kHz to 0.01 Hz. The specific capacity (C_m) was calculated from GD curves by the following equation

$$C_m = \frac{I \times \Delta t}{3.6 \times m} \tag{1}$$

where I (A) is the discharging current, Δt (s) is the discharging time, and m (g) is the mass of the active material. All electrochemical tests were carried out in a 6 M KOH electrolyte.

2.4. Capacitor Assembly and Photovoltaic Device Parameters. Asymmetric capacitors were assembled with $Ni(OH)_2$-rGO composite materials as the positive electrode and commercial activated carbon as the negative electrode. Both positive and negative electrodes of symmetrical capacitors were commercial activated carbon. The mass balance of the positive and negative electrodes is determined by the following equation

$$\frac{m_+}{m_-} = \frac{C_- \times \Delta V_-}{C_+ \times \Delta V_+} \tag{2}$$

where m_+/m_-, C_+/C_-, and $\Delta V_+/\Delta V_-$ are the mass, specific capacity, and working potential window of the positive/negative electrodes, respectively. Galvanostatic charge/discharge curves were measured using an electrochemical workstation (CHI660E, Chenhua) at a current density of 2 $A \cdot g^{-1}$.

The energy density (E) and power density (P) of the capacitors were calculated by the following equations

$$E = \frac{I \times \int V \, dt}{3.6 \times m} \tag{3}$$

$$P = \frac{3600 \times E}{t} \tag{4}$$

where I (A) is the discharging current, V (V) is the potential, m (g) is the total mass of the active material, and t (s) is the discharging time.

The photovoltaic part is a triple junction series connected to a PERC solar cell. $J-V$ and $P-V$ curves were measured by a source meter (Keithley 2400) under AM 1.5 G irradiation (100 $mW \cdot cm^{-2}$) from a solar light simulator (XES-301S + EL-100). The maximum power conversion efficiency (MPCE) of the PERC solar cell is 24.67%, the open-circuit voltage is 1.9 V, the short-circuit current

https://doi.org/10.1021/acsami.2c23046
ACS Appl. Mater. Interfaces 2023, 15, 11875−11884

density (J_{SC}) is 19.67 mA·cm^{-2}, and the maximum power point voltage is 1.54 V.

2.5. PRD Measurement and Calculations. The PRD was fabricated by the PERC solar cell as the photovoltaic part and symmetric/asymmetric capacitors as the energy storage part. All active materials of the positive electrode in energy storage parts had the same mass, and the mass of the negative electrode was matched according to eq 2. Under the irradiation of sunlight, the energy storage part was directly charged by the photovoltaic part used as a power supply, and the $V-t$ curve was recorded by an electrochemical workstation. Under dark conditions, the photovoltaic part and the energy storage part were disconnected, and the GD curve of the energy storage part was recorded. In addition, since the same photovoltaic device was used for testing, the constant-current discharge current of five types of energy storage parts was the same (10 mA).

The incident light energy (E_{light}) was calculated by the following equation

$$E_{light} = P_{light} \times S \times t \quad (5)$$

where P_{light} is the incident light power density (100 mW·cm^{-2}), S is the effective light area (3.26 cm^2) of the PRD, and t (s) is the photocharging time.

The actual power conversion efficiency of the photovoltaic part in the PRD (η_{pv}), the energy efficiency of the energy storage part in the PRD (η_{es}), and the overall efficiency of the PRD (η_{oa}) are calculated by the following equations

$$\eta_{pv} = \frac{E_{ie}}{E_{light}} = \frac{\int P_{ie}\,dt}{E_{light}} \quad (6)$$

$$\eta_{es} = \frac{E_{es}}{E_{ie}} = \frac{E_{es}}{\int P_{ie}\,dt} \quad (7)$$

$$\eta_{oa} = \frac{E_{es}}{E_{light}} \quad (8)$$

where E_{ie} is the input energy of the energy storage part, equal to the actual output energy of the photovoltaic part during the photocharging process, calculated according to the real-time $P-t$ curve of the PRD. E_{es} is the discharge energy of the energy storage part, calculated by the $P-t$ curve during dark discharging.

3. RESULTS AND DISCUSSION

High efficiency and easy preparation are two important characteristics of practical PRDs, while the selection of PV and ES parts can significantly affect the two characteristics. The PERC solar cell shows a high MPCE and outstanding stability, which is employed as the PV part. The supercapacitor is used as the ES part because of the simple structure, ease of preparation, and high-power density. The PRD is assembled for obtaining high efficiency, and the structure and working process are shown in Scheme 1. The solar energy is converted into electric energy after irradiating the PV part. Subsequently, the electric energy is converted into chemical energy and stored in the ES part through the charging process, and then it is converted into electric energy again through the discharging process. In the operation of the PRD, the actual power conversion efficiency of the PV part is called η_{pv} and the actual energy efficiency of the ES part is called η_{es}. Correspondingly, the power conversion efficiency at the maximum power point in the independent operation of the PV device is denoted as MPCE, and the energy efficiency of the ES device in the galvanostatic charge and discharge is called η_{ee}.

In recent years, the MPCE of PV devices has been greatly improved, but the η_{pv} is far from the MPCE. PV parts do not work stably at the maximum power point during photocharging, leading to $\eta_{pv} \leq$ MPCE. So, it is an effective way to improve the η_{oa} of the PRD by controlling η_{pv} as close to MPCE as possible. On the basis of this strategy, the relationship between the charging curve of the ES part and the $J-V$ curve of the PV part is studied and the following strategy is proposed.

Scheme 1. Illustration of the Structure and Energy Exchange Process of a PRD

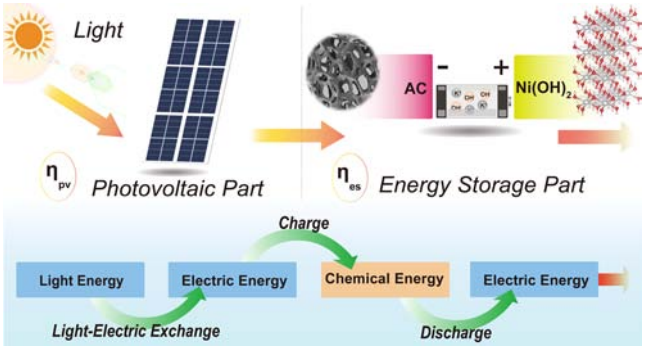

3.1. Strategy of Voltage Match on the Maximum Power Point. On the basis of the $J-V$ curve of the PV device, it can be known that the current of the PV device changes little before reaching the maximum power point, meanwhile the power keeps increasing during the voltage rise. The current and power of the PV device gradually decrease with the increase of the voltage after reaching the maximum power point. Therefore, to obtain the maximum power conversion efficiency, it is necessary to control the PV part to work near the maximum power point. For asymmetric capacitors using battery-type electrodes and some lithium- and sodium-ion batteries, there is usually a section of the charging curve where the voltage rises rapidly and the capacity rises less.[20,27,28] Then, there is another section where the capacity rises rapidly and the voltage changes little. The slopes of $V-t$ curves between the two sections are obviously different. The dividing point between the two sections can be called the inflection point, and the corresponding voltage is called V_{ip}. As shown in Figure 1a, the section of the $V-t$ curve in which the voltage is lower or higher than the V_{ip} is called the voltage segment (V segment) or the capacity segment (C segment), respectively. If the maximum power point of the PV part can be located in the C segment during the photocharging process, the PV part can work near the maximum power point, then the ideal η_{pv} is obtained. The fully charged voltage of the PRD is defined as V_{max}, and the maximum power point voltage of the PV device is defined as V_{mpp}. Obviously, V_{max} is higher than V_{ip}. Thus, there are three situations corresponding to the three relationships of voltage as follows

$$V_{max} > V_{mpp} > V_{ip} \quad (a)$$

$$V_{mpp} > V_{max} > V_{ip} \quad (b)$$

$$V_{max} > V_{ip} > V_{mpp} \quad (c)$$

Situations I, II, and III are caused by the different relationships among the V_{max}, V_{mpp}, and V_{ip}. Situation I corresponding to Inequality (a) is shown in Figure 1a. At the moment of illumination, the voltage of the PRD starts to rise. Due to the small capacity of the V segment, the voltage of the

https://doi.org/10.1021/acsami.2c23046
ACS Appl. Mater. Interfaces 2023, 15, 11875−11884

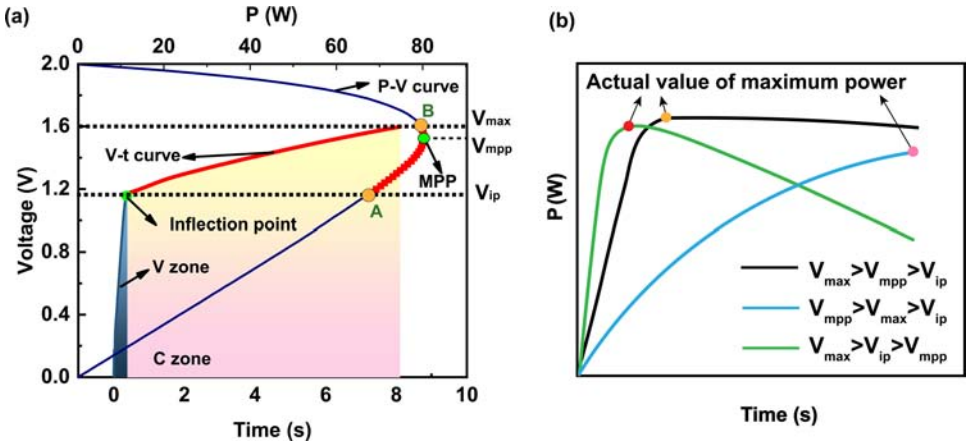

Figure 1. (a) $P-V$ curve of the PV device and the $V-t$ curve of the ES part in the PRD. (b) $P-t$ diagram of the PV part.

PRD quickly reaches V_{ip}. After the inflection point, the device enters the near-maximum power state. At this moment, the power of the PV part rises to a relatively high value with the voltage increase, and the ES part enters the C segment with a large capacity and small voltage change. Due to the control of voltage, there is a high output power of the PV part continuing to the end of the photocharging process. Moreover, the voltage change of the PV part is small, and the working state is relatively stable after the inflection point. To further improve the η_{pv}, the gap among V_{max}, V_{mpp}, and V_{ip} can be narrowed as much as possible. The most ideal situation, which is shown in Figure 1b as a black curve, is that the three kinds of voltage meet the Inequality (a) with a minimal difference. The blue curve in Figure 1b exhibits Situation II corresponding to Inequality (b). The output power of the PV part increases and is less than that of Situation I in the whole process. For Situation III corresponding to Inequality (c), the working state of the PV parts exceeded the actual maximum power point after reaching the C segment. Therefore, the output power increases in a short time to the maximum value, and drops immediately, corresponding to the green curve in Figure 1b. Both of the Situations II and III cause the working state of the PV part to deviate far from the maximum power point, so the η_{pv} is lower than that in Situation I. When the voltage is higher than the V_{ip}, the state of the PRD is defined as the near-maximum power state (NS). The PRDs were prepared based on the SVM as follows. The PERC solar cell was used as the PV part. The Ni-based materials and activated carbon (AC) were employed as electrodes of supercapacitors, which were used as the ES part. Abbreviations of the relevant nomenclature are shown in Table 1.

3.2. Construction of the Energy Storage Part. With high theoretical capacity, low cost, and environmental friendliness, $Ni(OH)_2$ is used as the positive material of an asymmetric capacitor. Using $NiSO_4{\cdot}6H_2O$, NaOH, and graphene oxide (GO), which can reduce the internal resistance, as raw materials the $Ni(OH)_2$-rGO composite material (GN1, GN2, and GN3, $Ni(OH)_2$ content increases in sequence) and pure $Ni(OH)_2$ (NH) for the positive electrode of the asymmetric capacitor were obtained by a simple hydrothermal method.

XRD patterns can be used to describe the phase and crystal structures of electrode materials. Figure 2 shows the XRD diffraction patterns of GN1, GN2, GN3, and NH. All diffraction peaks have been marked. Nine characteristic peaks

Table 1. Abbreviations of the Relevant Nomenclature

nomenclature	abbreviations
photorechargeable device	PRD
strategy of voltage match on the maximum power point	SVM
simplified device	SD
complete device	CD
photovoltaic	PV
energy storage	ES
maximum power conversion efficiency	MPCE
near maximum power state	NS
actual power conversion efficiency of photovoltaic part (in photorechargeable device)	η_{pv}
energy efficiency of the energy storage device	η_{ee}
actual energy efficiency of the energy storage part (in photorechargeable device)	η_{es}
voltage of the inflection point	V_{ip}
voltage of the maximum power point	V_{mpp}
fully charged voltage of the energy storage device	V_{max}
overall efficiency of the photorechargeable device	η_{oa}

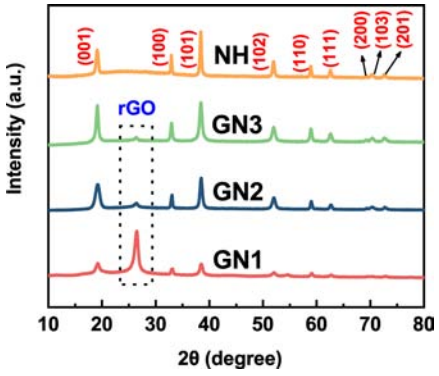

Figure 2. XRD patterns of GN1, GN2, GN3, and NH.

are observed for $Ni(OH)_2$-rGO composites and $Ni(OH)_2$ nanosheet samples, at 19.2, 33.0, 38.5, 52.0, 59.0, 62.7, 69.3, 70.3, and 72.7° corresponding to (001), (100), (101), (102), (110), (111), (200), (103), and (201) diffraction planes of β-$Ni(OH)_2$ (JCPDS 14-0117), which is consistent with previous literature.[29,30] With the increase of nickel dosage, the (002) peak intensity of rGO decreases gradually compared with the (101) peak intensity of $Ni(OH)_2$, which means that the number of exposed crystal planes of $Ni(OH)_2$ increases.

https://doi.org/10.1021/acsami.2c23046
ACS Appl. Mater. Interfaces 2023, 15, 11875−11884

Figure 3 shows the SEM images of the four as-prepared materials. In Figure 3a,b, it can be clearly seen that $Ni(OH)_2$

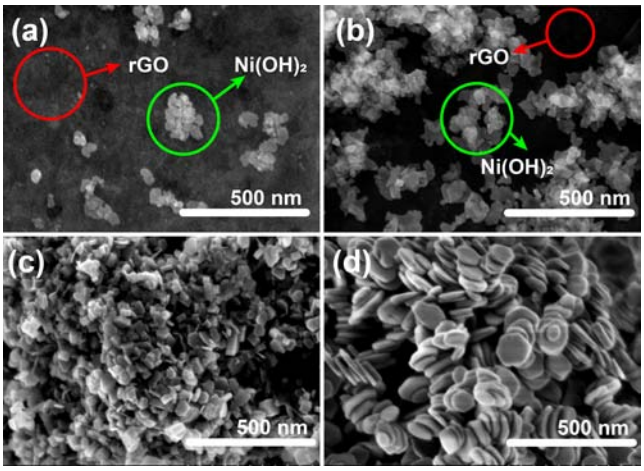

Figure 3. SEM images of (a) GN1, (b) GN2, (c) GN3, and (d) NH.

nanosheets grow on the surface of the rGO substrate, and the nickel source ($NiSO_4{\cdot}6H_2O$ and NaOH) dosage of GN1 is lower than that of GN2, so there are fewer $Ni(OH)_2$ nanosheets on the surface. Figure 3c,d shows the surface morphology of GN3 and NH, and both of them are $Ni(OH)_2$ nanoparticles without obvious rGO. The particles of GN3 are irregular in shape, while NH nanoparticles are hexagonal and significantly larger than GN3. For the four as-prepared materials, with the increase of nickel source dosage, the size of $Ni(OH)_2$ increases and its proportion increases. The increase of $Ni(OH)_2$ particle size and the decrease of rGO proportion will lead to the increase of the internal resistance for the materials.

The electrochemical behavior was examined by the CV test at 5 $mV{\cdot}s^{-1}$ and is shown in Figure 4a. The CV curves of all of the four electrodes have a relatively clear pair of redox peaks, which come from the reaction:[31] $OH^- + Ni(OH)_2 \rightarrow NiOOH + H_2O + e^-$. The CV curve of GN2 has the largest area corresponding to the largest specific capacity, while the CV curve of NH has the smallest area corresponding to the smallest specific capacity. The main reason is that GN2 has a suitable ratio of $Ni(OH)_2$ and rGO, and as the substrate, rGO can rapidly export electrons.[32] Figure 4b shows the EIS curves of the four electrodes. The first intersection of the curve and the real axis corresponds to the equivalent series resistance of the electrodes, which is composed of the solution resistance of the electrolyte, the intrinsic resistance of the active material as well as the contact resistance at the electrode and electrolyte interface.[33] Due to the poor conductivity of $Ni(OH)_2$, the equivalent series resistance of NH is significantly higher than that of the other three electrodes. However, the equivalent series resistance of the three composite electrodes is similar due to the outstanding conductivity of the rGO substrate.[34,35] The semicircle in the high-frequency region of the curve corresponds to the charge transfer resistance, which is mainly related to the resistance of the redox reaction. There is a significant semicircle area in the corresponding curve of NH, which means that the NH has a large charge transfer resistance.[36] The main reason is that $Ni(OH)_2$ has poor conductivity, and it is difficult to export electrons during the electrochemical reaction. GN1 also has a relatively small semicircle, which is probably due to the minimum NaOH dosage in the hydrothermal process and incomplete reduction of rGO, leading to the relatively weak conductivity of GN1, compared with GN2 and GN3. The slope of the low-frequency curve is mainly related to the capacitance characteristic of the electrode,[36,37] and the larger slope of the curve, the more the capacitance characteristic. With the increase of $Ni(OH)_2$ loading, the capacitance characteristic of the electrodes gradually weakened, which made the slope of the low-frequency region of the corresponding curves of the four electrodes gradually decrease.

Using the galvanostatic charge−discharge test (GCD) to characterize the capacity of electrodes, the galvanostatic discharge curves of the four kinds of electrodes are shown in Figure 4c and the galvanostatic discharge curves of AC are shown in Figure S1. The capacity of the composite electrodes is mainly provided by $Ni(OH)_2$, but its high internal resistance leads to serious loss in the discharge process. The actual capacity differs greatly from the theoretical capacity. It can reduce the capacity loss by loading $Ni(OH)_2$ on the rGO substrate with high conductivity. The internal resistance of GN3 is large and its capacity is lower than that of GN2 due to the excessive $Ni(OH)_2$ load. The galvanostatic discharge curves of the GN2 electrode at different discharge rates are shown in Figure 4d, and the specific capacity has been marked out. Due to the suitable ratio of $Ni(OH)_2$ and rGO, the specific capacity of GN2 reaches 332.17 $mAh{\cdot}g^{-1}$ at a current density of 2 $A{\cdot}g^{-1}$. When the current density is up to 50 $A{\cdot}g^{-1}$, the specific capacity is still up to 165.69 $mAh{\cdot}g^{-1}$, and the retention rate is nearly 50%.

The GCD of asymmetric capacitors was carried out to describe the charging inflection points. Figure 4e,f shows the GCD curves of the corresponding asymmetric capacitors, and the charging inflection points have been marked. The galvanostatic charge curve of the AC symmetrical capacitor has two sections, which is mainly caused by the relatively high current density of 2 $A{\cdot}g^{-1}$. For asymmetric capacitors with GN1, GN2, GN3, and NH as positive electrodes, the electrolyte and negative electrodes are the same, and the difference of inflection point voltages in the charge curve is mainly affected by the relative content of $Ni(OH)_2$ and rGO in the positive electrode materials.[38] NH is pure $Ni(OH)_2$, and the inflection point voltage of the asymmetric capacitor with NH as the positive electrode is the highest. The existence of the rGO conductive substrate in GN1, GN2, and GN3 reduces the internal resistance of the composite electrode, making its charging process easier than that of NH, which can utilize more active materials and reduce its inflection point voltage.[39−41] For GN1, the low content of $Ni(OH)_2$ is dispersed and anchored on the surface of rGO in a mosslike distribution, and it has good contact with rGO, leading to the low internal resistance of the composite. Due to the high electronic conductivity of rGO, the charge transfer process of GN1 easily reacts, which is reflected in the low inflection point in the galvanostatic charge curve.[42,43] With the increase of $Ni(OH)_2$ content, the $Ni(OH)_2$ in GN2 is granular. $Ni(OH)_2$ in GN3 became larger and thicker, and a large number of $Ni(OH)_2$ nanosheets grew on the rGO, showing obvious stacking, which weakened the contribution of rGO to the conductivity and increased the internal resistance of the composite materials. At the same time, its thicker $Ni(OH)_2$ nanosheets will hinder the insertion and removal of protons, which is not conducive to the occurrence of the oxidation−

https://doi.org/10.1021/acsami.2c23046
ACS Appl. Mater. Interfaces 2023, 15, 11875−11884

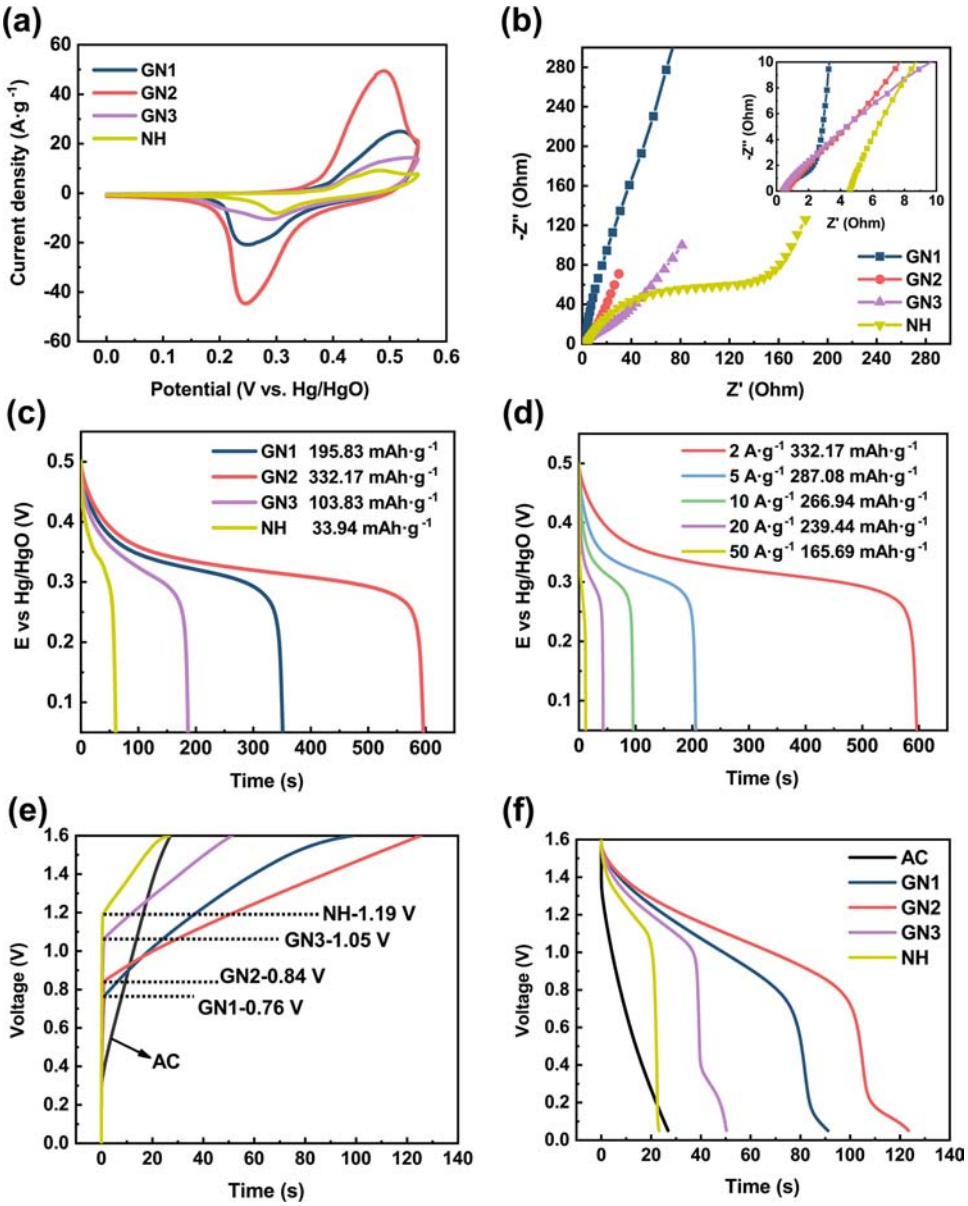

Figure 4. (a) CV curves at 5 mV·s^{-1}, (b) Nyquist plots, and (c) discharge curves of GN1, GN2, GN3, and NH. (d) Discharge curves of GN2 at different current densities. (e) Charge curves with inflection points of AC, GN1, GN2, GN3, and NH-based supercapacitors. (f) Discharge curves of AC, GN1, GN2, GN3, and NH-based supercapacitors.

reduction reaction, which is reflected in the increase of the inflection point in the galvanostatic charge curve.[44] In general, the charging process of the asymmetric capacitor shows that the content of $Ni(OH)_2$ in composite materials raised will cause the rise of the inflection point. The GN2-based asymmetric capacitor obtained 36.25 Wh·kg^{-1} energy density at 1057.38 W·kg^{-1} power density and the NH-based symmetric capacitor obtained 8.42 Wh·kg^{-1} energy density at 1307.03 W·kg^{-1} power density, and the detailed data are shown in Table 2.

3.3. Performance of the Photorechargeable Device. To describe the photovoltaic performance of the PERC solar cell, the $J-V$ and $P-V$ curves are shown in Figure 5a. The MPCE of the PV device is 24.67% and the V_{mpp} is 1.54 V. Taking an NH-based PRD as an example, Figure 5b describes the output power of the PV part and the voltage of the PRD during the photocharging process. It demonstrated that the V_{ip} of the NH-based PRD is 1.35 V, and the time from the start of illumination to the inflection point of the PRD is defined as t_{ss}, which is only 0.09 s. That is, the PV part reaches NS in about 0.09 s during the photocharging process of NH-based PRDs. At this moment, the output instantaneous power of the PV part is 74.29 mW, meanwhile, the maximum power during the charging process is 75.30 mW. The entire charging process is 4.63 s, which proves that the photocharging process is carried

Table 2. Energy Densities and Power Densities of AC, GN1, GN2, GN3, and NH-Based Supercapacitors

sample	energy density (Wh·kg^{-1})	power density (W·kg^{-1})
AC	4.77	640.05
GN1	27.40	1083.27
GN2	36.25	1057.38
GN3	24.68	1121.99
NH	8.42	1307.03

https://doi.org/10.1021/acsami.2c23046
ACS Appl. Mater. Interfaces 2023, 15, 11875−11884

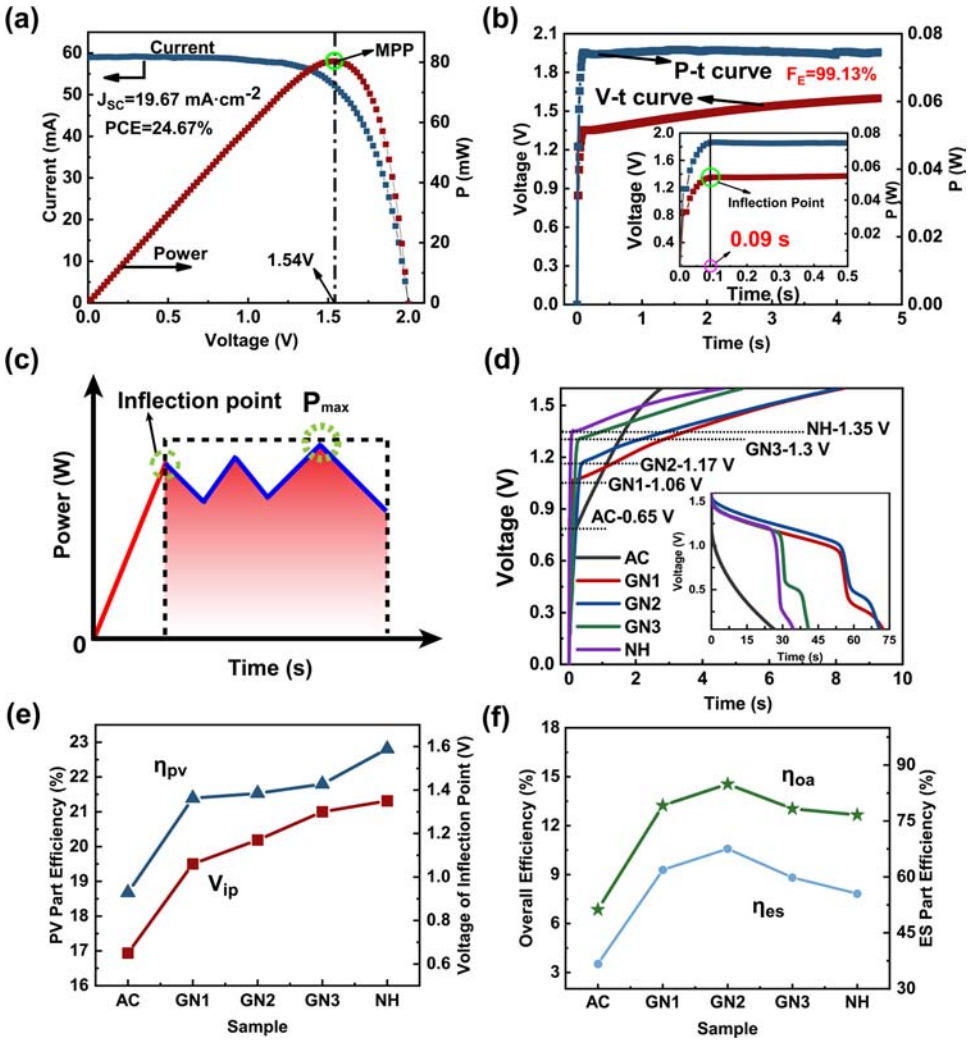

Figure 5. (a) $J-V$ and $P-V$ curves of the PERC solar cell. (b) $V-t$ and $P-t$ curves of the NH-based PRD during photocharging. The inset is the enlarged inflection point part. (c) Diagram of E_c and E_{max}. (d) Photocharging and dark discharging (inset) curves of five types of PRD. (e) η_{pv} and inflection point of five types of PRD. (f) η_{oa} and η_{es} of five types of PRD.

out at a relatively high rate. The $V-t$ and $P-t$ curves of a GN2-based PRD during photocharging are shown in Figure S2. In addition, the actual output energy of the PV part in the C segment during the photocharging process is defined as E_c, P is the instantaneous power of the PV part in the photocharging process, and t_c is the illumination time of the C segment

$$E_c = \int P \, dt_c \tag{9}$$

E_{max} is defined as the product of the actual value of the maximum power (P_{max}) and t_c in the photocharging process. To investigate the stability of the output power of the PV part in the photocharging process entering the C segment, the E fill factor (F_E) is defined as

$$F_E = E_c/E_{max} \tag{10}$$

For clearer understanding, the diagram of E_c and E_{max} is shown in Figure 5c. The solid line is the $P-t$ diagram, and the inflection point position has been marked out. Then, E_c refers to the area enclosed by the blue solid line and the coordinate axis. The black dotted line parallel to the horizontal axis crosses the maximum power point of the PV part. Therefore, E_{max} refers to the area enclosed by the three dotted lines and the horizontal axis. Figure 5d shows the photocharging and dark discharging curves of the PRD. The corresponding inflection points have been marked in this figure. The V_{max} of all five types of supercapacitors is 1.6 V, which is higher than the V_{mpp} of 1.54 V. The F_E values of the four types of asymmetric capacitors are all higher than 95%, which means that the asymmetric-capacitor-based PRD can work stably near the actual value of the maximum power during the photocharging process.

F_M is used to describe the deviation degree of the PRD from the maximum power state during the photocharging process

$$F_M = \eta_{pv}/\mathrm{MPCE} \tag{11}$$

Due to the well-designed inflection point voltage, the F_M of the NH-based PRD is up to 92.44%, which is very close to the MPCE of the PV device. It means that the PV part almost constantly works at the maximum power point during the photocharging process. Meanwhile, the F_M of the other three types of asymmetric-capacitor-based PRDs can also reach 85% or higher. However, the F_M of the AC-based PRD is only 75.73%. The F_M of the four types of asymmetric-capacitor-based PRDs are significantly higher than that of the AC-based PRD because there are a significant C segment and V segment

https://doi.org/10.1021/acsami.2c23046
ACS Appl. Mater. Interfaces 2023, 15, 11875−11884

Table 3. Data of Photorechargeable Devices in Photocharging and Dark Discharging

sample	η_{oa}	η_{pv}	η_{es}	F_M	F_E	t_{ss}
AC-based PRD	6.85%	18.68%	36.66%	75.73%	87.16%	
GN1-based PRD	13.24%	21.39%	61.89%	86.72%	95.71%	0.12 s
GN2-based PRD	14.55%	21.53%	67.57%	87.27%	96.83%	0.4 s
GN3-based PRD	13.04%	21.80%	59.83%	88.35%	98.34%	0.3 s
NH-based PRD	12.66%	22.81%	55.50%	92.44%	99.13%	0.09 s

in the four types of asymmetric capacitors, and the V_{ip} increases with the increase of $Ni(OH)_2$ content. According to the SVM, the V_{ip} of the four types of asymmetric-capacitor-based PRDs are controlled below the V_{mpp}, which should be as close to the V_{max} as possible. The V_{mpp} and V_{max} in this work are 1.54 and 1.60 V, respectively, with a difference of only 0.06 V. Therefore, as V_{ip} approaches V_{mpp}, η_{pv} approaches MPCE, which means the closer the F_M is to 100%.

The V_{ip} and η_{pv} are shown in Figure 5e. The related data in the photocharging process are shown in Table 3. The η_{oa}, η_{pv}, η_{es}, V_{ip}, and t_{ss} represent the overall efficiency, power conversion efficiency of the PV part in the PRD, the energy efficiency of the ES part in the PRD, inflection point voltage, and the time from the illumination time to the inflection point of the PRD, respectively. Compared with similar works using converters, which need 1 s or more time to reach the NS, in this work, the maximum value of t_{ss} is 0.4 s and the minimum value is only 0.09 s, which has significant advantages.[20,27] The above experimental results prove that the match between the V_{ip} and the V_{mpp} is an effective means to improve the η_{pv} in the PRD.

The η_{oa} of the five types of PRD is shown in Figure 5f. Due to the low η_{es} of the NH electrode, which is caused by the low conductivity, the η_{oa} is 12.66%, which is slightly lower than that of the GN2-based PRD up to 14.55%. Using SVM for device selection, the PV part can work near the maximum power point by adjusting the charging characteristics of the ES part. As a consequence, the SVM can improve the η_{pv}, thus improving the η_{oa}. Therefore, the usage of this strategy can greatly improve the practicality of the PRD.

4. CONCLUSIONS

In summary, the strategy of voltage match on the maximum power point for a PRD is proposed. The V_{mpp} of the PV part is matched with the V_{max} and the V_{ip} of the ES part, so that the PV part works in the NS during photocharging, and a higher η_{pv} and η_{oa} are realized. The PRD is assembled based on the proposed strategy. A PERC solar cell is employed as the PV part with a V_{mpp} of 1.54 V. An asymmetric capacitor with a V_{max} of 1.6 V is used as the ES part. $Ni(OH)_2$-rGO composite materials and pure $Ni(OH)_2$ are used as positive electrodes of asymmetric capacitors. The V_{ip} is adjusted by changing the content of $Ni(OH)_2$ and rGO to make it close to the V_{mpp}. Benefiting from the SVM, a GN2-based PRD shows a maximum η_{oa} of 14.55% and only takes 0.4 s to reach the NS. The η_{pv} and F_M of the GN2-based PRD are as high as 21.53 and 87.27%, respectively. The strategy can not only improve the η_{pv} but also guide the selection of the PV and ES parts in PRD.

■ ASSOCIATED CONTENT

Supporting Information

The Supporting Information is available free of charge at https://pubs.acs.org/doi/10.1021/acsami.2c23046.

Discharge curves of AC at different current densities and $V-t$ and $P-t$ curves of the GN2-based PRD (PDF)

■ AUTHOR INFORMATION

Corresponding Author

Meicheng Li − *State Key Laboratory of Alternate Electrical Power System with Renewable Energy Sources, School of New Energy, North China Electric Power University, Beijing 102206, China*; orcid.org/0000-0002-0731-741X; Email: mcli@ncepu.edu.cn

Authors

Binglin Guo − *State Key Laboratory of Alternate Electrical Power System with Renewable Energy Sources, School of New Energy, North China Electric Power University, Beijing 102206, China*

Yongyue Li − *State Key Laboratory of Alternate Electrical Power System with Renewable Energy Sources, School of New Energy, North China Electric Power University, Beijing 102206, China*

Yihao Gao − *State Key Laboratory of Alternate Electrical Power System with Renewable Energy Sources, School of New Energy, North China Electric Power University, Beijing 102206, China*

Shengnan Zhao − *State Key Laboratory of Alternate Electrical Power System with Renewable Energy Sources, School of New Energy, North China Electric Power University, Beijing 102206, China*

Yingfeng Li − *State Key Laboratory of Alternate Electrical Power System with Renewable Energy Sources, School of New Energy, North China Electric Power University, Beijing 102206, China*

Xiaojun Lv − *State Key Laboratory of Alternate Electrical Power System with Renewable Energy Sources, School of New Energy, North China Electric Power University, Beijing 102206, China*

Changhua Mi − *State Key Laboratory of Alternate Electrical Power System with Renewable Energy Sources, School of New Energy, North China Electric Power University, Beijing 102206, China*

Complete contact information is available at: https://pubs.acs.org/10.1021/acsami.2c23046

Author Contributions

B.G.: conceptualization, methodology, experiment, and writing the original draft; Y.L.: experiment, writing−review, and editing; Y.G.: writing−review and editing; S.Z.: experiment and review; Y.L.: writing−review and editing; X.L.: supervision and writing−review; C.M.: experiment and editing; and M.L.: conceptualization, supervision, writing−review, and editing.

Notes

The authors declare no competing financial interest.

https://doi.org/10.1021/acsami.2c23046
ACS Appl. Mater. Interfaces 2023, 15, 11875−11884

■ ACKNOWLEDGMENTS

This work is supported partially by the Project of State Key Laboratory of Alternate Electrical Power System with Renewable Energy Sources (LAPS21004, LAPS202114), the Natural Science Foundation of Hebei (E2022502022), National Natural Science Foundation of China (Grant nos. 52272200, 51972110, 52102245, and 52072121), Beijing Science and Technology Project (Z211100004621010), Beijing Natural Science Foundation (2222076, 2222077), Huaneng Group Headquarters Science and Technology Project (HNKJ20-H88), 2022 Strategic Research Key Project of Science and Technology Commission of the Ministry of Education, China Postdoctoral Science Foundation (2022M721129) and the Fundamental Research Funds for the Central Universities (2022MS030, 2021MS028, 2020MS023, 2020MS028), and the NCEPU "Double First-Class" Program.

■ REFERENCES

(1) Smalley, R. E. Future Global Energy Prosperity: The Terawatt Challenge. *MRS Bull.* **2005**, *30*, 412−417.
(2) Hashemi, S. A.; Ramakrishna, S.; Aberle, A. G. Recent Progress in Flexible-Wearable Solar Cells for Self-Powered Electronic Devices. *Energy Environ. Sci.* **2020**, *13*, 685−743.
(3) Schmidt, D.; Hager, M. D.; Schubert, U. S. Photo-Rechargeable Electric Energy Storage Systems. *Adv. Energy Mater.* **2016**, *6*, No. 1500369.
(4) Xue, H.; Gong, H.; Yamauchi, Y.; Sasaki, T.; Ma, R. Photo-Enhanced Rechargeable High-Energy-Density Metal Batteries for Solar Energy Conversion and Storage. *Nano Res. Energy* **2022**, *1*, No. e9120007.
(5) Wu, Y. H.; Li, C.; Tian, Z. N.; Sun, J. Y. Solar-Driven Integrated Energy Systems: State of the Art and Challenges. *J. Power Sources* **2020**, *478*, No. 228762.
(6) Gurung, A.; Qiao, Q. Q. Solar Charging Batteries: Advances, Challenges, and Opportunities. *Joule* **2018**, *2*, 1217−1230.
(7) Wang, L.; Wen, L.; Tong, Y.; Wang, S.; Hou, X.; An, X.; Dou, S. X.; Liang, J. Photo-Rechargeable Batteries and Supercapacitors: Critical Roles of Carbon-Based Functional Materials. *Carbon Energy* **2021**, *3*, 225−252.
(8) Dong, W. J.; Cho, W. S.; Lee, J. L. Indium Tin Oxide Branched Nanowire and Poly(3-hexylthiophene) Hybrid Structure for a Photorechargeable Supercapacitor. *ACS Appl. Mater. Interfaces* **2021**, *13*, 22676−22683.
(9) Zheng, X.; Sun, Y.; Qin, H.; Ji, Z. Solar-Charged Pseudocapacitors: Simultaneous Conversion and Storage of Solar Energy in ZnO@NiO Nanorod Arrays. *J. Alloys Compd.* **2019**, *781*, 351−356.
(10) Zhu, K.; Zhu, G.; Wang, J.; Zhu, J.; Sun, G.; Zhang, Y.; Li, P.; Zhu, Y.; Luo, W.; Zou, Z.; Huang, W. Direct Storage of Holes in Ultrathin $Ni(OH)_2$ on Fe_2O_3 Photoelectrodes for Integrated Solar Charging Battery-Type Supercapacitors. *J. Mater. Chem. A* **2018**, *6*, 21360−21367.
(11) Wang, P.; Chen, X. T.; Sun, G. Z.; Wang, C.; Luo, J.; Yang, L. Q.; Lv, J.; Yao, Y. F.; Luo, W. J.; Zou, Z. G. A Capacitor-Type Faradaic Junction for Direct Solar Energy Conversion and Storage. *Angew. Chem., Int. Ed.* **2021**, *60*, 1390−1395.
(12) Xu, R.; Pan, J.; Wu, B.; Li, Y.; Wang, H. E.; Zhu, T. Fabrication of Zn-Cu-Ni Ternary Oxides in Nanoarrays for Photo-Enhanced Pseudocapacitive Charge Storage. *Nanomater.* **2022**, *12*, 2457.
(13) Zhu, T.; Pan, J.; An, Z.; Zhe, R.; Ou, Q.; Wang, H.-E. Bifunctional $NiCuO_x$ Photoelectrodes to Promote Pseudocapacitive Charge Storage by *in situ* Photocharging. *J. Mater. Chem. A* **2022**, *10*, 20375−20385.
(14) Lau, D.; Song, N.; Hall, C.; Jiang, Y.; Lim, S.; Perez-Wurfl, I.; Ouyang, Z.; Lennon, A. Hybrid Solar Energy Harvesting and Storage Devices: The Promises and Challenges. *Mater. Today Energy* **2019**, *13*, 22−44.
(15) Zeng, Q.; Lai, Y.; Jiang, L.; Liu, F.; Hao, X.; Wang, L.; Green, M. A. Integrated Photorechargeable Energy Storage System: Next-Generation Power Source Driving the Future. *Adv. Energy Mater.* **2020**, *10*, No. 1903930.
(16) Cohn, A. P.; Erwin, W. R.; Share, K.; Oakes, L.; Westover, A. S.; Carter, R. E.; Bardhan, R.; Pint, C. L. All Silicon Electrode Photocapacitor for Integrated Energy Storage and Conversion. *Nano Lett.* **2015**, *15*, 2727−2731.
(17) Keppetipola, N. M.; Tada, K.; Olivier, C.; Hirsch, L.; Bessho, T.; Uchida, S.; Segawa, H.; Toupance, T.; Cojocaru, L. Comparative Performance Analysis of Photo-Supercapacitor Based on Silicon, Dye-Sensitized and Perovskite Solar Cells: Towards Indoor Applications. *Sol. Energy Mater. Sol. Cells* **2022**, *247*, No. 111966.
(18) Yuan, Y. L.; Wu, Y. H.; Zhang, T.; Tang, H. C.; Meng, L.; Zeng, Y. J.; Zhang, Q. H.; Ye, Z. Z.; Lu, J. G. Integration of Solar Cells with Hierarchical CoS_x Nanonets Hybrid Supercapacitors for Self-Powered Photodetection Systems. *J. Power Sources* **2018**, *404*, 118−125.
(19) Li, T.-T.; Yang, Y.-B.; Zhao, B.-S.; Wu, Y.; Wu, X.-W.; Chen, P.; Gao, X.-P. Photo-Rechargeable All-Solid-State Lithium-Sulfur Batteries Based on Perovskite Indoor Photovoltaic Modules. *Chem. Eng. J.* **2022**, *455*, No. 140684.
(20) Kin, L.-c.; Liu, Z.; Astakhov, O.; Agbo, S. N.; Tempel, H.; Yu, S.; Kungl, H.; Eichel, R.-A.; Rau, U.; Kirchartz, T.; Merdzhanova, T. Efficient Area Matched Converter Aided Solar Charging of Lithium Ion Batteries Using High Voltage Perovskite Solar Cells. *ACS Appl. Energy Mater.* **2020**, *3*, 431−439.
(21) Gurung, A.; Chen, K.; Khan, R.; Abdulkarim, S. S.; Varnekar, G.; Pathak, R.; Naderi, R.; Qiao, Q. Highly Efficient Perovskite Solar Cell Photocharging of Lithium Ion Battery Using DC-DC Booster. *Adv. Energy Mater.* **2017**, *7*, No. 1602105.
(22) Li, W.; Jin, S. Design Principles and Developments of Integrated Solar Flow Batteries. *Acc. Chem. Res.* **2020**, *53*, 2611−2621.
(23) Hu, Y. X.; Bai, Y.; Luo, B.; Wang, S. C.; Hu, H.; Chen, P.; Lyu, M. Q.; Shapter, J.; Rowan, A.; Wang, L. Z. A Portable and Efficient Solar-Rechargeable Battery with Ultrafast Photo-Charge/Discharge Rate. *Adv. Energy Mater.* **2019**, *9*, No. 1900872.
(24) Li, W. J.; Fu, H. C.; Zhao, Y. Z.; He, J. H.; Jin, S. 14.1% Efficient Monolithically Integrated Solar Flow Battery. *Chem* **2018**, *4*, 2644−2657.
(25) Song, Z.; Wu, J.; Tu, Y.; Sun, L.; Zhu, T.; Li, G.; Wang, X.; Du, Y.; Deng, C.; Chen, Q.; Sun, W.; Huang, M.; Fan, L.; Huang, Y.; Wei, Y.; Xie, Y.; Lin, Y.; Chen, H.; Lin, J.; Zhan, L.; Gao, P.; Nazeeruddin, M. K.; Huang, W. Photocapacitor Integrating Voltage-Adjustable Hybrid Supercapacitor and Silicon Solar Cell Generating a Joule Efficiency of 86%. *Energy Environ. Sci.* **2022**, *15*, 4247−4258.
(26) Agbo, S. N.; Merdzhanova, T.; Yu, S. C.; Tempel, H.; Kungl, H.; Eichel, R. A.; Rau, U.; Astakhov, O. Development towards Cell-to-Cell Monolithic Integration of a Thin-Film Solar Cell and Lithium-Ion Accumulator. *J. Power Sources* **2016**, *327*, 340−344.
(27) Gurung, A.; Reza, K. M.; Mabrouk, S.; Bahrami, B.; Pathak, R.; Lamsal, B. S.; Rahman, S. I.; Ghimire, N.; Bobba, R. S.; Chen, K.; Pokharel, J.; Baniya, A.; Laskar, M. A. R.; Liang, M.; Zhang, W.; Zhang, W. H.; Yang, S.; Xu, K.; Qiao, Q. Rear-Illuminated Perovskite Photorechargeable Lithium Battery. *Adv. Funct. Mater.* **2020**, *30*, No. 2001865.
(28) Wang, Z. R.; Chiu, H. C.; Paolella, A.; Zaghib, K.; Demopoulos, G. P. Lithium Photo-Intercalation of CdS-Sensitized WO_3 Anode for Energy Storage and Photoelectrochromic Applications. *ChemSusChem* **2019**, *12*, 2220−2230.
(29) Zhu, J.; Chen, S.; Zhou, H.; Wang, X. Fabrication of a Low Defect Density Graphene-Nickel Hydroxide Nanosheet Hybrid with Enhanced Electrochemical Performance. *Nano Res.* **2012**, *5*, 11−19.
(30) Mao, Y.; Xie, J.; Liu, H.; Hu, W. Hierarchical Core-Shell Ag@$Ni(OH)_2$@PPy Nanowire Electrode for Ultrahigh Energy Density Asymmetric Supercapacitor. *Chem. Eng. J.* **2021**, *405*, No. 126984.
(31) Yan, J.; Fan, Z. J.; Sun, W.; Ning, G. Q.; Wei, T.; Zhang, Q.; Zhang, R. F.; Zhi, L. J.; Wei, F. Advanced Asymmetric Supercapacitors Based on $Ni(OH)_2$/Graphene and Porous Graphene

https://doi.org/10.1021/acsami.2c23046
ACS Appl. Mater. Interfaces 2023, 15, 11875−11884

Electrodes with High Energy Density. *Adv. Funct. Mater.* **2012**, *22*, 2632−2641.
(32) Wang, H.; Song, Y.; Liu, W.; Yan, L. Three Dimensional $Ni(OH)_2$/rGO Hydrogel as Binder-Free Electrode for Asymmetric Supercapacitor. *J. Alloys Compd.* **2018**, *735*, 2428−2435.
(33) Sun, H.; Cao, L.; Lu, L. Bacteria Promoted Hierarchical Carbon Materials for High-Performance Supercapacitor. *Energy Environ. Sci.* **2012**, *5*, 6206−6213.
(34) Zhao, B.; Zhang, L.; Zhang, Q.; Chen, D.; Cheng, Y.; Deng, X.; Chen, Y.; Murphy, R.; Xiong, X.; Song, B.; Wong, C.-P.; Wang, M.-S.; Liu, M. Rational Design of Nickel Hydroxide-Based Nanocrystals on Graphene for Ultrafast Energy Storage. *Adv. Energy Mater.* **2018**, *8*, No. 1702247.
(35) Bai, J. W.; Yan, H. J.; Liu, Q.; Liu, J. Y.; Li, Z. S.; Bai, X. F.; Li, R. M.; Wang, J. Synthesis of Layered α-$Ni(OH)_2$/RGO Composites by Exfoliation of α-$Ni(OH)_2$ for High-Performance Asymmetric Supercapacitors. *Mater. Chem. Phys.* **2018**, *204*, 18−26.
(36) Upadhyay, K. K.; Bundaleska, N.; Abrashev, M.; Bundaleski, N.; Teodoro, O. M. N. D.; Fonseca, I.; de Ferro, A. M.; Silva, R. P.; Tatarova, E.; Montemor, M. F. Free-Standing N-Graphene as Conductive Matrix for $Ni(OH)_2$ Based Supercapacitive Electrodes. *Electrochim. Acta* **2020**, *334*, No. 135592.
(37) Chen, R.; Ling, H.; Huang, Q.; Yang, Y.; Wang, X. Interface Engineering on Cellulose-Based Flexible Electrode Enables High Mass Loading Wearable Supercapacitor with Ultrahigh Capacitance and Energy Density. *Small* **2022**, *18*, No. e2106356.
(38) Zhang, C.; Chen, Q.; Zhan, H. Supercapacitors Based on Reduced Graphene Oxide Nanofibers Supported $Ni(OH)_2$ Nanoplates with Enhanced Electrochemical Performance. *ACS Appl. Mater. Interfaces* **2016**, *8*, 22977−22987.
(39) Fang, D.-L.; Chen, Z.-D.; Liu, X.; Wu, Z.-F.; Zheng, C.-H. Homogeneous Growth of Nano-Sized β-$Ni(OH)_2$ on Reduced Graphene Oxide for High-Performance Supercapacitors. *Electrochim. Acta* **2012**, *81*, 321−329.
(40) Tessier, C.; Haumesser, P. H.; Bernard, P.; Delmas, C. The Structure of $Ni(OH)_{2.}$ From the Ideal Material to the Electrochemically Active One. *J. Electrochem. Soc.* **1999**, *146*, 2059.
(41) Wang, K.; Zhang, X.; Zhang, X.; Chen, D.; Lin, Q. A Novel $Ni(OH)_2$/Graphene Nanosheets Electrode with High Capacitance and Excellent Cycling Stability for Pseudocapacitors. *J. Power Sources* **2016**, *333*, 156−163.
(42) Chen, X.; Chen, X.; Zhang, F.; Yang, Z.; Huang, S. One-Pot Hydrothermal Synthesis of Reduced Graphene Oxide/Carbon Nanotube/α-$Ni(OH)_2$ Composites for High Performance Electrochemical Supercapacitor. *J. Power Sources* **2013**, *243*, 555−561.
(43) Jiang, Y.; Song, Y.; Li, Y.; Tian, W.; Pan, Z.; Yang, P.; Li, Y.; Gu, Q.; Hu, L. Charge Transfer in Ultrafine LDH Nanosheets/Graphene Interface with Superior Capacitive Energy Storage Performance. *ACS Appl. Mater. Interfaces* **2017**, *9*, 37645−37654.
(44) Ma, X.; Li, Y.; Wen, Z.; Gao, F.; Liang, C.; Che, R. Ultrathin β-$Ni(OH)_2$ Nanoplates Vertically Grown on Nickel-Coated Carbon Nanotubes as High-Performance Pseudocapacitor Electrode Materials. *ACS Appl. Mater. Interfaces* **2015**, *7*, 974−979.

https://doi.org/10.1021/acsami.2c23046
ACS Appl. Mater. Interfaces 2023, 15, 11875−11884